aerospace

MDPI

Article

Development of Carbon Composite Blades within the Context of the Experimental Validation of a CFD-Based Design Tool for Contra-Rotating, Electric Fan Engines

Sebastian Hawner *,†, Lukas Rduch, Henry Baumhöfener and Andreas Hupfer

Institute of Aeronautical Engineering, University of the Bundeswehr Munich, 85579 Neubiberg, Germany; lukasrduch@web.de (L.R.); henry.baumhoefener@unibw.de (H.B.); andreas.hupfer@unibw.de (A.H.)

* Correspondence: sebastian.hawner@unibw.de; Tel.: +49-89-6004-7209

† Current address: Institute of Aeronautical Engineering, Willy-Messerschmitt-Straße 1, 82024 Taufkirchen, Germany.

Abstract: Electric propulsion systems have emerged as a disruptive technological approach towards achieving sustainable and climate-neutral aviation. To expand the operational envelope of such propulsion units in terms of altitude and velocity, an enclosing duct and counter-rotating rotors to enhance efficiency can be utilized. In this study, an iterative CFD-based design tool developed for these novel propulsion systems is utilized to design a reference engine, having a classic rotor–stator configuration. Being the key component of this propulsor, a manufacturing process for composite blades is presented. This effort aims to make state-of-the-art technology accessible to smaller research projects, promoting the widespread adoption of electric propulsion technology in the aviation sector. By experimental investigations of the blade elongation both in tensile tests and engine operation, measuring the tip clearance with a high-speed camera, this process could be validated to facilitate the transferability of research. Finally, the performance of the manufactured engine is measured by a five-hole miniature probe, not only in design point but also in off-design operation. The results indicate that a substantial reduction in discrepancies between initial specifications, subsequent CFD simulations, and experimental investigations compared to conventional design tools relying on empirical formulations can be achieved due to the CFD-based approach. This allows the CFD-based tool to be validated for designing scalable contra-rotating fan engines.

Keywords: contra-rotating propulsor; CFD-based design tool; composite fan blades; electric fan engine

Citation: Hawner, S.; Rduch, L.; Baumhöfener, H.; Hupfer, A. Development of Carbon Composite Blades within the Context of the Experimental Validation of a CFD-Based Design Tool for Contra-Rotating, Electric Fan Engines. *Aerospace* **2024**, *11*, 527. https://doi.org/10.3390/aerospace11070527

Academic Editor: Jun Huang

Received: 16 May 2024
Revised: 21 June 2024
Accepted: 21 June 2024
Published: 27 June 2024

1. Introduction

By 2021, traffic already accounted for 24% of the global direct CO_2 emissions, despite the influence of the COVID-19 pandemic, with aviation contributing 2.5% presently [1,2]. Given that aviation falls into the category of "hard-to-abate" sectors in terms of CO_2 emission reduction, its share of the overall CO_2 emissions is expected to reach 11% within the next two decades [3]. This anticipation is magnified by current research results indicating that aircraft emissions' impact on the anthropogenic greenhouse effect should be weighted two to three times higher than that of ground-based transportation due to the high-altitude operation [4–6]. Despite a partial shift of passenger volume towards more efficient modes of transport, such as trains for short- and medium-haul distances, an additional annual increase of approximately 5% in transport volume is anticipated for the upcoming years. Due to the contrast to the incremental improvement of fuel consumption per seat of current gas turbine engines, which is projected to increase slightly from 2% to only 2.2% by 2034 [7], it becomes imperative to consider disruptive approaches like full-electric or hybrid concepts to achieve the ambitious goals of the *Flightpath 2050* or the *European Green Deal* [8,9]. Though these innovative strategies have already been demonstrated in general

recently [10,11], they demand a substantial increase in gravimetric energy and power density to enhance competitiveness. However, they might offer several advantages, such as enabling synergies between the engines and other aircraft components. For instance, the integration of distributed, high-dynamic propulsion systems can lead to reductions in the size and resulting drag of control surfaces.

Regarding the actual propulsor, most current research is focused on replacing traditional propeller drives of general aviation aircraft with electric motors. Since electric aircraft are also mainly evaluated based on economic and operational criteria, achieving high flight speeds is crucial for most scenarios. In response to this, a ducted, contra-rotating electric fan engine is being developed and investigated within the project *ELAPSED (Electrified Aircraft Propulsion safe, efficient, digitally linked)* as a part of the *digitalization and technology research center dtec.bw* of the *Federal Armed Forces of Germany* [12]. This innovative approach can be a response to the expectation that the demand for electric aircraft engines is expected to surpass the typical flight speed range of propellers. To expand the operation range beyond their limit of low to medium flight Mach numbers, a ducting system along with a high total pressure ratio across the fan stage of the propulsor is applied instead. The increased specific thrust enables small cross-sections, typically prescribed by the aircraft concept anyway, and compact engine designs, crucial for high flight speeds, as the drag increases quadratically with the speed. Furthermore, when powering such a fan system by electric motors, the application of contra-rotating stages become a feasible option to increase the efficiency, investigated within the project but not considered here initially.

Returning to the already discussed required increase in power density, the application of lightweight structures like composite blades made of carbon fiber-reinforced plastics (CFRPs) offers tremendous potential. While this technology already represents a state-of-the-art solution for large engines, for instance, within the *GE 90* [13], it has seen limited application in the academic and research-intensive context due to the increased manufacturing complexity. To enhance the transferability of research findings, especially regarding the areas of heat management of electrified aircraft engines or the application of active tip clearance control systems, a less labor-intensive manufacturing process for composite fan blades will be developed and validated by combining various innovative approaches, including tensile testing.

Furthermore, as already introduced previously in [14], an innovative design tool for ducted, electric fan engines was developed within the project. Common preliminary design tools are typically based on empiric formulations that are most often valid for a certain input range only. For instance, *Carter's rule* [15,16] and extensions built upon this foundation [17–19] are typically applied to account for deviation angles in axial turbomachinery. However, these parametrized formulations are limited to a certain range of their input parameters and most often valid for large engines. Therefore, their application for smaller engines like within the scope of this project, for instance, as required for the already discussed distributed propulsion concepts, cause significant deviations between the initial engine specification, on the one hand, and the *CFD* (*computational fluid dynamics*) calculations as well as the experimental results on the other hand. In contrast to blades having a large tip-to-hub ratio, the outflow of the small blades designed here is dominated by 3D effects that seem to be not properly incorporated into the empiric formulations. Within a former project, such an empiric correlation-based design tool was developed at the institute and utilized to design an electric, ducted engine. However, the experimental investigations confirmed relatively large deviations between the initial specification and the subsequent CFD simulation and experimental investigation [20–22]. To enable the accurate design of freely scalable drives, the application of the empiric correlations is replaced by the incorporation of CFD. Since the computing power increased substantially during recent years, for instance, by the introduction of high-performance clusters at universities, this approach became a feasible option for preliminary design tools, as shown here as well. Nevertheless, the effort, as expected, is larger for designing the engine due to the iterative character.

Summarizing, two major research questions are to be answered in the following. First, is it possible to validate the design tool with a manufactured engine? Can it be verified that the CFD approach, as anticipated, increases the accuracy and reduces the deviations between the initial specification and the numerical as well as the experimental results? And second, can a feasible manufacturing process for composite blades be found and validated? Whereas it has to be suitable for an application within a research context at universities where both the financial resources and the manufacturing capacities are strictly limited, it must not compromise the tool validation nonetheless.

2. Methods: Application of the Developed Tool to Design a Reference Propulsion System

The design tool, initially introduced in [14] and further explained with the example below, should be verified and validated by designing a *reference propulsion system (RPS)* and its subsequent experimental investigation. In order to focus on the tool's functionality, the RPS contains a common rotor–stator stage. However, the functionality of the design of various sub-components, like the composite blades or the disk, and the manufacturing of 3D-printed components, like the nozzle or the standard inlet, should be verified within the RPS to enable their similar application within the future *innovative propulsion system (IPS)*, having a contra-rotating stage. Furthermore, this reduces the complexity of the validation process of this initial step, as the total pressure distribution has to be measured and compared at a single engine stage only compared to the two positions after each rotor of the IPS later. In principle, the automated tool chain, shown in Figure 1, is based on an iterative, CFD-based calculation of initially unknown parameters like the rotor's isentropic compressor efficiency or total pressure losses over inlet, stator, and nozzle.

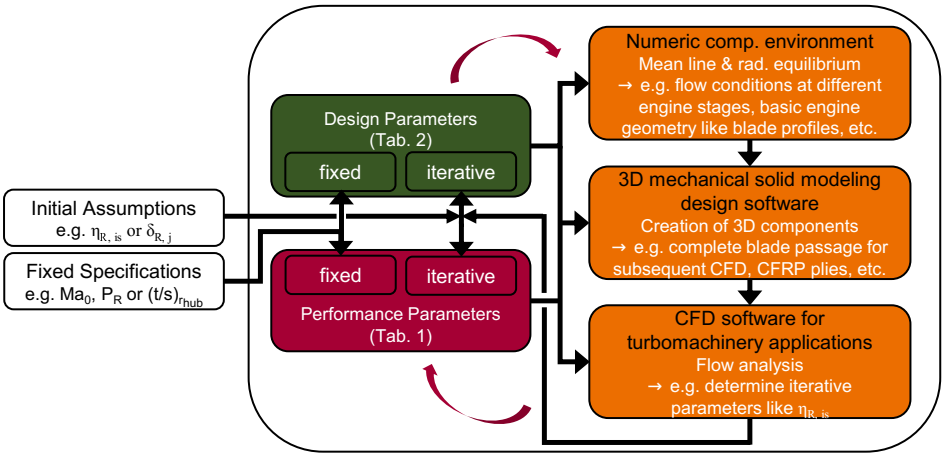

Figure 1. Toolchain of the developed engine design tool, adapted from the initial introduction in [14].

The inputs into the tool can be split up into the two categories: *performance* and *design* parameters. Due to the tool's iterative character, both categories contain not only fixed parameters but also values that require initial assumptions at the beginning, replaced by CFD results for later iterations. The main entries of the first category and their chosen values for the RPS design are summarized in Table 1 and discussed in the following.

The actual calculation part of the toolchain mainly consists of three parts, indicated by the individual orange boxes on the right-hand side of Figure 1. Within a numeric computing environment, the first step is to determine the general design of the various components, like the blades, standard inlet, casing, or nozzle. By a mean line approach, the values of (total) pressure p_t and (total) temperature T_t are calculated from the performance parameters, among others, from the total pressure ratios π_i. They relate the total pressure conditions before and after a certain component. For instance, the fixed total pressure ratio

over the rotor π_R specifies the ratio of the total pressure p_t at the rotor's outlet to its value at the inlet, indicated by the subscripts 1.1 and 1.2, respectively, as follows:

$$\pi_R = \frac{p_{t,1.2}}{p_{t,1.1}}. \quad (1)$$

The total pressure losses over inlet, stator, and nozzle, given by the respective total pressure ratios π_{inlet}, π_{stator}, and π_{nozzle} and defined similar to that of the rotor, enable the determination of the total pressure at all engine stages. However, as indicated in Table 1, they have to be determined iteratively by the CFD later, in contrast to the fixed value of π_R. The flight Mach number, $Ma_0 = 0$, results from the planned tool validation by a static engine operation within the test bed set up at the institute. Together with an altitude specification, the inlet total pressure $p_{t,0}$ and temperature $T_{t,0}$, as well as the static outlet pressure p_0, are set, based on the *International Standard Atmosphere* [23]. By the assumption of an adiabatic inlet, stator, and nozzle, and by incorporating the isentropic efficiency $\eta_{R,is}$, the total temperature at all stages can be determined, too. The difference in total temperature over the rotor is used, in these terms, to determine the required specific work for the specified total pressure ratio. Together with the available motor's shaft power P_R and further specifications like axial flow Mach numbers at different stages or hub radii, this allows the calculation of the engine's mass flow and general radii. Afterwards, *Euler's turbine equation* is utilized to calculate the required flow deflection from the determined specific work and rotation speed input n_R. Finally, a radial equilibrium is implemented to calculate the flow angles not only at the mean line radius but also at all other radial positions.

Table 1. Extraction of the fixed and iterative performance parameters of the reference propulsion system, sorted in order of their utilization.

Parameter	(Final) Value	Unity	Category
Ma_0	0	–	fixed
π_R	1.063	–	fixed
π_{inlet}	0.9994	–	iterative
π_{stator}	0.9983	–	iterative
π_{nozzle}	0.9992	–	iterative
$\eta_{R,is}$	0.9392	–	iterative
P_R	14,093	W	fixed
n_R	14,487	rpm	fixed
$Ma_{1.1}$	0.2	–	fixed

The value of 1.063 chosen for the total pressure ratio π_{R1} facilitates a comparability to current developments of electric, ducted propulsion systems. In contrast to fans of state-of-the-art aircraft engines, reaching values up to 1.7, it appears to be relatively low. However, this enables, in these terms, relatively low rotation speeds without avoiding undercutting recommendations like a *DeHaller number* > 0.7 across the entire span. Subsequently, the strength requirements regarding the blades are relatively low in the first place for the RPS to gain experience for scaling it later within the IPS. The stage inflow Mach number $Ma_{1.1}$ at the engine's mean line had to be found as a trade-off between the Mach number-dependent *DeHaller* number and radial blade length. The minimal *DeHaller* number of 0.746 occurs at the hub, increasing to 0.812 at the mean line and 0.859 at the shroud, based on the mentioned *radial equilibrium approach* and the chosen *free vortex design principle*. Due to the low Mach numbers set inside the engine and the low total pressure ratio, a high isentropic efficiency, and small total pressure losses within inlet, the stator and nozzle could be found

iteratively. The range of the motor's shaft power was chosen with regard to the maximum output power of the installed power supply within the test bed of 15.3 kW.

Furthermore, it includes margins for testing at speeds larger than design point speed and the estimated losses within the motor and its *electronic speed controller (ESC)*.

Whereas the performance parameters rather describe the actual engine cycle, based on the flight mission and deployment scenario, the group of design parameters contains specifications that finalize the engine's design within the first part of the design tool, affecting the engine's performance.The most important parameters of this category are summarized in Table 2.

Table 2. Extraction of the fixed and iterative design parameters of the reference propulsion system.

Parameter	(Final) Value	Unity	Category
$t/s\,(r_{hub})$	0.765	–	fixed
$t/s\,(r_{ML})$	0.9	–	fixed
$t/s\,(r_{shroud})$	1.035	–	fixed
$d_{max}/s_{\mathrm{R}}\,(r_{hub})$	0.07	–	fixed
$d_{max}/s_{\mathrm{R}}\,(r_{shroud})$	0.03	–	fixed
$i_{B,rotor}$	11	–	fixed
$i_{B,stator}$	6	–	fixed
$\mathrm{AS_R}$	15	mm	fixed
$\mathrm{TC_R}$	0.5	mm	fixed
$\delta_{\mathrm{R},hub}$	15	deg	iterative
$\delta_{\mathrm{R},ML}$	6.5	deg	iterative
$\delta_{\mathrm{R},shroud}$	1.3	deg	iterative

In contrast to the iterative performance parameters, representing global specifications, the iterative design parameter deviation angle $\delta_{R,j}$ must be specified for the three radial positions j meanline (ML), hub, and shroud. All radial positions in between are linearly interpolated to find $\delta(r)$. Their values must be iteratively adjusted so that the initially specified, global performance parameter total pressure ratio π_{R} and its corresponding total pressure increase $\Delta p_{t,R1}$ over the rotor are achieved within the subsequent CFD simulation. The actual metal angles $\beta_{\mathrm{K}}(r)$ of the blade's *NACA 65* profile [24] are increased from the original calculation, based on *Euler's turbine equation* and the *radial equilibrium*, by the found angles $\delta(r)$. The fixed parameters of this group are, apart from the tip clearance TC, based on findings of other, similar research activities. For instance, the number of the rotor blades i_{R} and the respective inverse of the solidity, t/s, the axial spacing between the rotor and stator $\mathrm{AS_R}$, and the maximum relative blade thickness d_{max}/s were chosen following the results of systematic experimental and numerical variations in [25–27]. Though all those investigations were made on contra-rotating stages, the findings were nevertheless adopted here to test all the designed engine components by a geometry close to that of the future IPS. To account for the varying deflection over the span, the solidity is adjusted by 15% towards hub and shroud to increase efficiency. Furthermore, the relative thickness is increased from shroud to hub to account for the increasing load. Since the manufacturing quality and, subsequently, the operational behavior of the blades were not known yet during input parameter specification, the tip clearance TC_{DP} was set relatively large, at 0.5 mm. For optimal results, all fixed values of both performance and design parameters would have to be varied, too, to find an optimal design. However, as for the RPS design, the validation of the tool is of utmost importance and not the optimization of the engine's performance itself; the parameters were not optimized at this point.

The general geometry, calculated within the actual iteration's first step from the input parameters, is subsequently utilized in a 3D mechanical solid modeling design software to generate the actual 3D components. This includes not only the actual blades of the rotor but also casing components like the nozzle or the standard inlet in accordance with *VDI*

ISO 5167 [28], taken over into the CFD analysis afterwards. For a more detailed description of the geometry calculation, refer to the previous publication in [14].

Within the third step, the engine's performance is investigated by a steady-state CFD simulation, focusing on the iterative parameters. In order to reduce the calculation effort, a single blade passage, created as negative from the *CAD* (*computer aided design*) components, is modeled by allying rotational periodicity at the domain boundaries in circumferential directions. Four stationary domains for inlet, stator, nozzle, and outlet as well as one rotating domain for the rotor are set up. The inlet includes an additional volume ahead of the actual beginning of the standard inlet, having an axial length and diameter of two and four times the rotor's outer diameter, respectively. Similar, the outlet enlarges the blade passage by the simulation of the free flow after the nozzle, where this volume has an axial length and diameter of three and four times the rotor's outer diameter. Furthermore, the nozzle's outer flow is included by enlarging this outlet domain upstream from the actual nozzle's outlet plane. At the interfaces between the domains themselves, the *mixing plane* approach is used by defining the corresponding pitch angles depending on the number of rotor and stator blades. Within the rotating rotor domain, the shroud's wall is set up as *contra-rotating*, as it does not rotate with the rotor. In contrast, the hub is included as a rotating wall. To account for friction effects, the *no slip wall* approach is utilized for all wall boundaries. Furthermore, all walls are set to be adiabatic. The application of inflation layers on all surfaces, including the in- and outlet, ensures a normalized wall distance $y+ <= 4$ to include boundary layer effects. In addition, the mesh is refined at all of these surfaces. Turbulence is included by the *Shear Stress Transport (SST)* approach, successfully demonstrated, for instance, in [20,29]. This k$-\omega$-based two-equation model seems to be a suitable trade-off between computing effort and accuracy. It offers a highly precise prediction of flow separation phenomena and was validated, among others, in [30], required for the simulation of throttled operation points investigated here. All outer boundaries are specified by the *entrainment* and *opening* pressure and temperature option to define them either as total or static values, depending on whether the surface permits flow into or out of the domain. Finally, the engine speed is set by the angular velocity of the rotor domain. During the actual iterative design process of the RPS, the compressible *Reynolds-averaged Navier–Stokes Equations*, implemented in *Ansys CFX*, are solved for a steady-state solution and the different variables, like total pressure ratios or efficiencies, are determined, mass flow-averaged in accordance with the implemented calculations used for the design tool.

Returning to the iterative adjustment of the design parameters discussed above, the upper part of Figure 2 visualizes the iterative adjustment of the deviation angle. Since the rotor was designed in accordance with the *free vortex design principle* to receive a constant increase in enthalpy over the span, the required fluid deflection at the hub is much larger than that at the shroud to balance out the lower circumferential speed of the blade at lower radial positions. Therefore, significant deviations between the desired and within-*CFX* simulated flow angles can be detected, especially close to the hub, resulting in a reduced increase in total pressure calculated by the CFD. As discussed above, in common design tools, the attempt to avoid this is the application of empiric correlations to determine the required corrections of the blade's trailing edge angle. In contrast, within the design tool approach discussed here, the three local deviation angles are adjusted from iteration step to step, as plotted in the upper part of Figure 2 in accordance with the results shown in Figure 2. Initial values were taken from the IPS design presented in [14]; due to design differences like other solidities, the final values differ. The minimization of the local deviations results in decreased deviation of the global specifications of the total pressure increase $p_{\Delta p_{t,\mathrm{R}}}$, as shown in the lower part of Figure 2 by the black curve. The deviations p of the other iterative, global performance parameters are calculated between the result of the actual and the previous iteration step, representing a rate of change. Similar to the resulting green curve of the deviation of the isentropic efficiency plotted within the lower part of Figure 2, these rates decline with increasing iteration steps. After the 16th iteration,

all deviations of the global performance parameters undercut the chosen abortion criterion of 0.1%. The final RPS geometry of this iteration is shown as a CAD rendering in Figure 3.

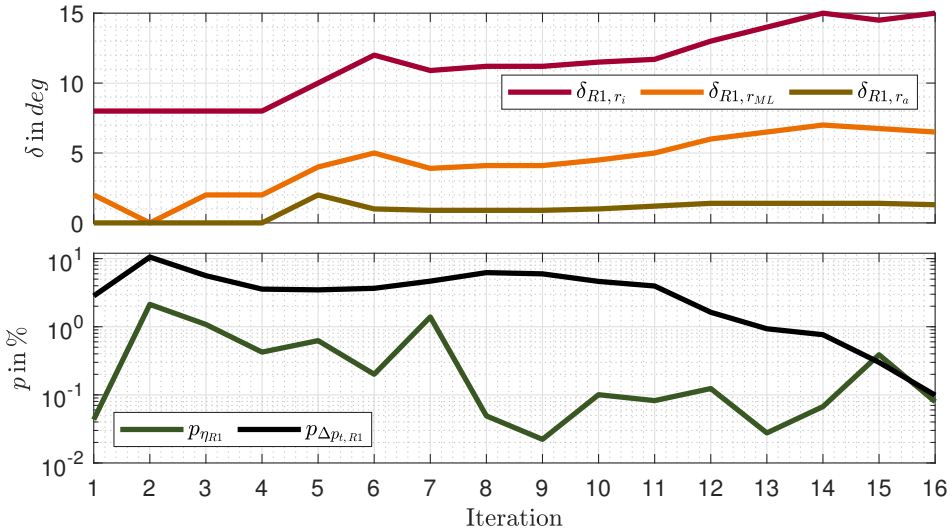

Figure 2. Adjustment of the local deviation angle δ and resulting deviation of the global performance parameters p (lower part) depending on the actual iteration.

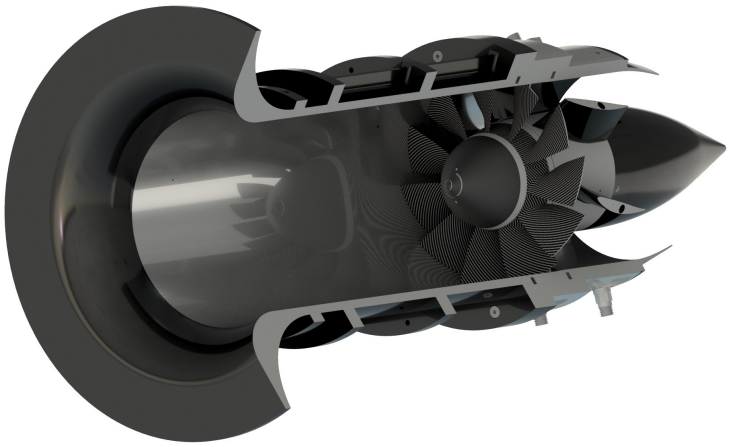

Figure 3. CAD rendering of the RPS in its final geometry of the 16th iteration.

Typically, the results of a CFD simulation depend on the quality of the applied mesh. Based on the previously mentioned requirement to undercut a $y+$ value of 4 on all surfaces, the first layer thickness of all inflation layers was set to 10 µm. In order to find suitable values for the general and the refinement element size, a systematic mesh convergence study was carried out, based on the *Richardson Extrapolation* [31]. The described blade passage was simulated by three different meshes at design speed; the results are summarized in Table 3.

All meshes are geometrically similar, as the refinements and inflation layers were placed in all cases on all surfaces. As prescribed in [31], an averaged volume element edge length h is calculated from the element number and total volume of the blade passage, used to ensure the meshes are refined by at least a factor of 1.3. For the convergence study, the simulated values of total pressure increase $\Delta p_{t,R1,0}$, mass flow $\dot{m}$, and isentropic rotor efficiency η_{R1} were considered. In contrast to the iterative design process, focusing on achieving the specified total pressure increase over the rotor $\Delta p_{t,R1}$, the experimental setup allows the measurement of the total pressure increase from ambient to the rotor's outlet plane only. Though this is explained in detail below in the context of the test bed description, this enlarged value is taken into account here already, indicated by the subindex 0. In

the order mentioned above, the apparent orders p of 7.19, 17.14, and 1.09 result for the considered outputs. Due to the small relative errors e_r and $e_{r,extr.}$ of the second simulated mesh, related to the finest mesh 3 and the extrapolated results, respectively, a further reduction in the element size did not seem to be meaningful. Furthermore, steady-state simulations of the blade passage in design point operation are carried out, as for the iterative design process. Not only that, but the performance map of the engine is also calculated by transient simulations to consider unsteady behavior, especially during throttling. These transient simulations require the simulation of two adjacent blade passages of all domains except for the stator. Since the number of rotor blades is nearly twice the number of stator blades, this ensures the required pitch ratio close to unity at all domain interfaces. Therefore, the number of elements for those transient simulations is approximately twice the number stated in Table 3. To find a trade-off between solution accuracy and computing effort, the second mesh was chosen for the later performance map simulations, resulting in slightly increased errors but halved element number compared to the finest mesh.

Table 3. Comparison of the simulation results in terms of relative and extrapolated relative errors for three different meshes.

Parameter	Mesh 1	Mesh 2	Mesh 3
Element No.	3.81 mio.	8.51 mio.	19.1 mio.
h	1.64 mm	1.26 mm	0.96 mm
$e_{r,\Delta p_{t,R1,0}}$	12.79%	1.62%	–
$e_{r,\dot{m}}$	7.05%	0.07%	–
$e_{r,\eta_{R1}}$	1.38%	0.59%	–
$e_{r,extra.,\Delta p_{t,R1,0}}$	13.02%	1.89%	0.27%
$e_{r,extra.,\dot{m}}$	7.05%	0.07%	<0.01%
$e_{r,extra.,\eta_{R1}}$	3.06%	2.29%	1.71%
$GCI_{fine,\Delta p_{t,R1,0}}$	2.72%	0.34%	–
$GCI_{fine,\dot{m}}$	0.09%	<0.01%	–
$GCI_{fine,\eta_{R1}}$	5.09%	2.17%	–

However, not only the local discretization but also the discretization in time has to be reviewed for transient simulations. It is specified by the simulated number of time steps per passing period which, in these terms, describes the duration of a rotor blade passing the following stator blade. Apart from the doubled blade passages for the majority of domains, the interfaces between the domains are changed to *transient rotor stator* for these simulations. Furthermore, the steady-state simulations are aborted if all root-mean-square residuals undercut a value of 10^{-5}.

For the transient calculations, the following two criteria have to be reached instead in accordance with typical recommendations for transient simulations. First, the arithmetic averages of the calculated mass flow and total pressure ratio over two intervals, one equaling a total, the other one a half revolution of the rotor, are within a relative tolerance. Second, the coefficients of variation of the same two outputs, calculated from the standard deviation divided by the mean, both considered over a whole revolution, have to be within a certan irelative tolerance, too. Adjusted for the case considered here, the solutions can be considered converged if a tolerance of 0.5% is undercut by both criteria, where the final outputs were calculated as the mean of the entire last revolution. Finally, for the selection of a suitable number of time steps per period, not only was the result accuracy reviewed, but so were nearly all time steps of the final revolution, to verify whether they undercut the same residual target of 10^{-5}, like the steady-state solutions. Three different numbers of time steps per period were considered, as summarized in Table 4.

Similar to the discussion of the local discretization above, relative errors e_r of the same three outputs, referring to the finest simulation of the third case, were calculated. Since

unsteady behavior is of relevance when simulating throttled behavior, not only simulations with the design nozzle, but also simulations with the outlet area reduced to 75% were considered here, too. Again, a trade-off was found in the second option of five time steps per period, as the deviations to the third case are small compared to the doubled computing effort.

Table 4. Comparison of the simulation results in terms of relative errors for three different considered cases, differing by the number of time steps per period.

Parameter	Case 1	Case 2	Case 3
Time Steps p. Period	1	5	10
$e_{r,\Delta p_{t,R1},75\%}$	4.17%	1.35%	–
$e_{r,\Delta p_{t,R1},100\%}$	0.93%	0.37%	–
$e_{r,\dot{m},75\%}$	0.49%	0.03%	–
$e_{r,\dot{m},100\%}$	0.65%	0.15%	–
$e_{r,\eta_{R1},75\%}$	2.07%	0.64%	–
$e_{r,\eta_{R1},100\%}$	0.5%	0.09%	–

Overall, it could be demonstrated that, as expected, the deviations between initial specification and CFD recalculations significantly decreased by directly incorporating CFD instead of relying on empirical formulations, while the effort increased due to the iterative nature.However, a final evaluation of the entire toolchain will only be possible during the experimental validation phase below, incorporating the influence of the composite manufacturing. To reduce the number of iterations, simple correlations could be implemented to obtain better initial values. Additionally, while reaching the global convergence limit is possible, adjusting only three radial positions seems insufficient to achieve the desired pressure rise across the entire span. Especially for the design of the future contra-rotating propulsor, local flow distortions would be critical, as they could lead to local flow separations at the subsequent second rotor. Therefore, the number of radial adjustment points should be increased. Based on the discussion of the discretization in time, a simulation option was found that seems to be suitable for calculating the entire performance map of the engine. Since the deviations between the steady-state and transient results account for 0.42%, 0.86%, and 0.52% regarding the result of total pressure increase, mass flow, and efficiency, the transient simulation seems to confirm the steady-state results. As, in addition, the computing effort is similar, a transient simulation could already be used for future iterative design processes. The final blade and overall engine geometry of the 16th iteration were later transferred into a manufacturable design, maintaining the aerodynamic surfaces and geometries. Apart from the composite blades, discussed in the following, the design of further components is summarized later.

3. Methods: Utilization of Carbon Composite Blades and Evaluation

The most significant advantage of using composite structures lies in the substantial reduction in weight, up to 70–80%, compared to traditional metallic blades. This reduction enables highly dynamic behavior and enhances the engine's gravimetric power density. Additionally, there is an increase in the blade's safety factor and a potential decrease of up to 40% in the maximum relative profile thickness, leading to aerodynamic advantages [32,33]. However, despite these advantages, the widespread adoption of composite blades faces certain challenges. Issues related to repairability and recycling remain open questions. Furthermore, the manufacturing process for composite blades is more complex and labor-intensive compared to traditional milling methods, relying heavily on manual craftsmanship. Consequently, the application of composite blades is currently limited and predominantly reserved for a few large-scale projects.

While research projects of a similar scale to the *ELAPSED* project are scarce, one noteworthy example is the *counter-rotating integrated shrouded propfan (CRISP)* project conducted

by *DLR* [34]. This project utilizes a standard structure of the individual composite plies for the two rotors, which deliver a pressure ratio of 1.3 at a mass flow rate of 130 kg/s. This employed structure adheres to a typical symmetrical layup of composite plies, allowing for quasi-isotropic properties. It consists of a symmetrical arrangement of 128 plies, following the $0° / \pm 45° / 90°$ orientation, forming an organo sheet. This sheet is subsequently subjected to hot forming and machined to achieve the desired contour. The primary load considerations for these blades, however, are radial and torsional stresses. Therefore, within the *CRISP* project, various approaches to numerically optimizing the layup configuration are being explored, enabling a reduction in the maximum displacement by up to 38% [35].

For the *ELAPSED* project, however, two approaches have been developed to enable the adoption of this technology in smaller research endeavors. Firstly, the development of a new design tool, as previously explained, has streamlined the direct and automated integration of both composite layers and moulding creation. This represents a significant departure from the previously intricate and time-consuming process of generating these layers and mouldings for existing designs created in different programs. In this context, where the contour or outer geometry of the blade is precisely known in the form of a point cloud and does not need to be separately imported or recreated, the design tool allows for the flexible calculation of the maximum local ply count based on the to-be-specified ply thickness and maximum relative blade thickness, both being input parameters for the design tool. Additionally, a fundamental layup configuration is embedded within the code. Since a common configuration of individual blades mounted on an inner disk was chosen, the blade consists not only of the actual blade, its upper part, but it includes a blade root as well. This lower part has a front and rear nose that are used to mount the blades into the disk's lugs.

As an example, the resulting ply structure of the blade's tip is shown in the left-hand part of Figure 4. It consists not only of the two outer plies, predefined by the aerodynamic surface, but also out of two inner layers on both suction and pressure sides, resulting in a total of six layers in its center. Since the blade's maximum thickness increases towards the hub, the number of plies in the transition from the actual blade to the root amounts to 12. As shown in the center of Figure 4, all layers do not end at the transition to the root but are wrapped around a carbon fleece utilized in the root. The layers are finally unwrapped within the CAD software to receive the individual 2D ply, shown on the right-hand side of Figure 4. All these steps described so far are included in the design tool described above and are processed automatically.

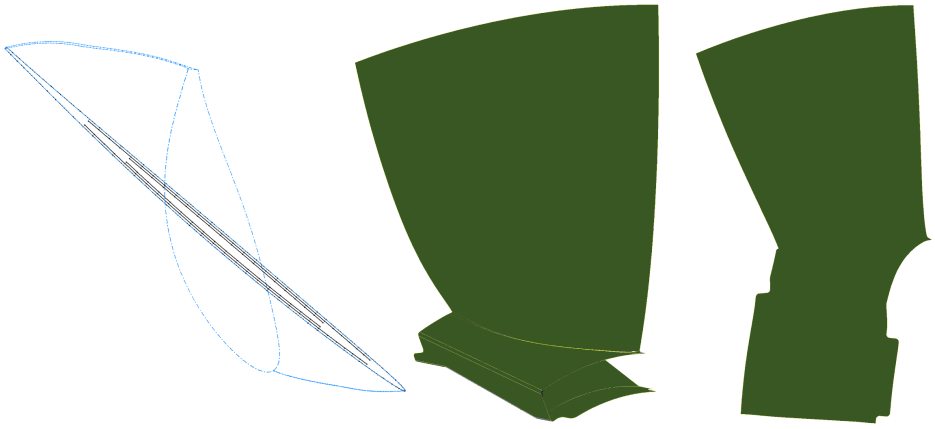

Figure 4. View of the blade tip's cross-sectional 3D point cluster (**left**), including those of two inner plies and the upper part of the outermost pressure- and suction-side plies (indicated in blue), shown also as 3D geometry and 2D unwrap (**center**, **right**).

The second approach developed in this context involves the utilization of cutting-edge *stereolithography (SLA)* 3D printing technology. Due to the intricate blade geometry, conventional composite manufacturing methods such as autoclave production were not

feasible options. Instead, the design tool automatically generates five moulding parts. Apart from the two main parts for both pressure and suction sides, based on the blade geometry's similarity to the creation of the individual plies, three further parts are used for the blade's root. To replace the costly and time-intensive milling procedures in the production of these mouldings, several 3D printing options were explored. However, due to the requirement for a smooth surface finish, *fused deposition modeling (FDM)* printers did not meet the criteria. Instead, *SLA* printers were employed, reducing the labor involved in moulding production significantly, as no further manual post-processing is required. The mouldings for the reference propulsion system blades were still produced using glass-reinforced resins. This material meets the strength requirements for moulding pressing but exhibited high brittleness. Consequently, the mouldings could only be used 2–3 times, and occasional chipping from the mouldings resulted in rejected blades. However, through systematic variation of post-curing duration and temperature on newer and even more cost-effective resins, followed by tensile and notch impact tests, the ductility and maximal elongation could be increased significantly, by a factor of five, even offering a smoother surface finish. The initial version with mouldings printed by an *FDM* printer, resulting in the uneven surface discussed above, compared to the final version of an RPS blade with a smooth surface, is presented in Figure 5. Since both blades are not used within the rotor, their small flaws on the surface are not post-treated by filling them with a mixture of resin and ground carbon fiber.

Figure 5. Initial (**left**) and final (**right**) versions of the composite blade.

Several tested *prepreg* materials did not yield satisfactory results because of the small radii within the transition zone. Instead, traditional dry 160 gm^{-2} *twill fabric* is employed. It is impregnated with the infusion resin *MGS RIMR426*, cut to match the 2*D* plies discussed earlier, and positioned into the mouldings via hand laminating. To accommodate torsion, the outermost plies are oriented at $\pm 45°$, while all inner plies are oriented at $\pm 90°$ relative to the radial direction. Subsequently, the five-part moulding is pressed together, and the blade cures initially at room temperature before being removed from the mouldings and tempered at 100 °C for another hour. Due to the anisotropic material behavior and the consequent need to model the individual plies and their interaction in an *FEM* (*finite element method*) analysis, such structural analysis regarding elongation and strength is considerably more complex compared to metallic materials, for example. Consequently, for the RPS, which experiences relatively low loads, this analysis was omitted and the already discussed ply orientation was chosen based on the findings in [35]. Instead, the tensile tests discussed below are intended to be used in the future for validating such a detailed FEM model. This validated model will then be employed to calculate the significantly more heavily loaded blades of the IPS prior to their production. However, different post-curing conditions of the blades were tested, resulting in the optimal tempering discussed above.

Apart from the eleven blades produced for the actual rotor, eighteen further blades were manufactured. Those were used, on the one hand, for initial tests regarding the

printer selection, based on the achievable surface smoothness. On the other hand, they were used for the following tensile and bending tests, including a variation of the blade's curing conditions. Since the overall production time could be reduced to 2 h per blade, this process seems to be an applicable option within the university context. However, the rotor should be used to validate the design tool. Consequently, any geometric deviations from the CAD could prove critical, potentially leading to discrepancies in behavior compared to the CFD calculations. Compared to the target maximum thickness of 1.93 mm at the blade's tip, the respective mean value measured amounts to 1.97 mm, having a standard deviation of 0.05 mm. Furthermore, the chord is measured to 57.63 mm at the blade's tip, with a standard deviation of 0.83 mm, whereas the target was 59.11 mm. This will be revisited during the tool validation later. To compensate for inequalities in the radial length of the blades, the entire rotor, with the finally assembled blades, was machined down to the desired outer radius in one step, with the radius determined based on the tensile tests and commissioning tests discussed in detail below. In addition to ensuring geometric reproducibility, which could thus be guaranteed, reproducibility of blade mass for balancing is crucial for rotor operation. Therefore, at least a static balancing could be carried out successfully, ensuring that the rotor's center of gravity lies within the engine axis. A balancing mass was applied under the base of all blades scheduled for the rotor operation after curing. This mass consists of the same resin material already used for the actual plies but was reinforced here with ground carbon fiber. Subsequently, material was removed from the balancing mass, again using a precision scale having an accuracy of 0.1 mg, resulting in an average blade mass m_b of 17,925.9 mg, with a very low standard deviation of 2.5 mg.

As previously mentioned, the tip clearance between the blade and casing at design point speed TC_{DP} is one of the input parameters for the design tool. While a smaller value enhances the blade's performance by reducing reverse flow and swirl effects, a certain margin must be maintained to prevent grinding of the blades at the casing, for instance, during maneuvers resulting in unexpected blade elongation effects. Given the anticipated relatively high E-modulus for composite blades, a moderate TC_{DP} of 0.5 mm has been selected. However, due to the radial loads caused by rotation, blade tip grinding is necessary to establish a specific TC_0 at $n = 0$ rpm, which then reduces to the chosen TC_{DP} with increasing engine speed. The blade elongation causing the reduction in tip clearance depends mainly on the material's *Young's modulus E*. Since composite belongs to the category of anisotropic materials, its *Young's modulus* in a particular considered direction, in this case the radial direction, is heavily influenced by the layer sequence and structure. Unlike isotropic materials, performing an FEM calculation to determine the anticipated elongation is projected to be quite resource-intensive. Furthermore, since this approach necessitates subsequent validation owing to the multitude of boundary conditions that need to be set, this step is omitted. Instead, the blade's performance is experimentally validated both by tensile and operational tests, discussed in the following, and the findings are leveraged to determine an expected blade elongation and a suitable TC_0.

As a basis for defining an appropriate testing procedure, a calculation of the expected blade loading is carried out. The blades are exposed to the centrifugal and aerodynamic forces. While the latter load is indicated by the subindex "*a*", a subindex for indicating centrifugal forces is omitted in the following for the sake of improved readability. First, the centrifugal force F caused by the actual blade is calculated, excluding the root, since it is clamped into the disk. At any radial position r_j between hub and shroud, r_{hub} and r_{shroud}, respectively, the effective force can be determined by integration, as follows:

$$F(\omega, r_j) = -\omega^2 \cdot \rho \int_{r_{shroud}}^{r_j} A(r) \cdot r \, dr. \tag{2}$$

The blade's cross-section $A(r)$ varies across the radius and is therefore set by the CAD data. Furthermore, a constant density ρ across the entire blade is assumed, calculated from

the measured mass and the CAD model volume.According to this approach, the maximum centrifugal force occurs at the transition into the foot:

$$F(\omega_{DP}, r_{hub}) = 1555\,\text{N} \tag{3}$$

where the angular velocity ω_{DP} corresponds to the design point speed of 14,487 rpm. With increasing radius, it diminishes, reaching zero at the blade's tip. Though, in contrast, the aerodynamic axial force of 14.68 N at design point, determined from the CFD simulation, is much smaller, the blade behavior under this load is experimentally tested, too.

Since the samples are not standardized, the testing procedure for the tensile test must be conducted in accordance with *DIN EN ISO 527-5* [36]. To facilitate the experiments in academic research, this test setup was chosen, as it is designed for a universal testing machine capable of operating in both tension and compression directions. The model used here for both tests is the *inspekt table* 50 kN by *Hegewald & Peschke*. It features wedge-screw grips on both the lower fixed and the upper movable traverse. The lower clamping of the blade is achieved by using a two-part holder, similar to the engine's disk, which is bolted to the lower traverse. An adapter for the upper traverse is utilized to avoid torsional moments on the blade caused by its twisted geometry. To clamp the curved and twisted tip surface using the jaws of the clamping tool, flat outer surfaces of the elements used to apply the forces are required. To mill the negative profiles of the blade's pressure and suction side, the manufacturing of these elements, as depicted in *DIN EN ISO 527-5*, is only partially feasible. Instead, their thickness had to be increased and the use of cross-laminated *glass-fiber reinforced plastic (GFRP)* fabrics is unsuitable due to the cutting of a significant portion of the fibers during the manufacturing process, leading to the loss of required properties. Given that *DIN EN ISO 527-5* mandates that the strength values and coefficient of variation must be at least equivalent to those of *GFRP*, the commonly used aviation-grade aluminum 7075 is employed. The stipulated radial extension of those profiles, 50 mm, is reduced to 20 mm to cover as little of the blade as possible while avoiding slipping. To enhance the coefficient of friction at the contact interface, the elements are subjected to *SiC* sandblasting. There is no adhesive bonding between the blades and the described elements. It is worth mentioning that the pressure-side element is additionally employed in the bending test to achieve a uniform load distribution on the blade tip.

This approach ensures that all carbon fibers are effectively stressed, thus closely simulating engine operational conditions.

The subsequently discussed test series was conducted on blades of identical design and curing conditions mentioned above and like the ones actually installed on the engine. In Figure 6, the measured absolute elongation Δs_i is plotted depending on the blade i and the applied force F. Upon examining this diagram, two distinct gradient regions become evident. While the slope is relatively shallow and intermittently wavering for forces $F < 2000$ N, a linear, steeper increase is observed above this threshold. The lower slope likely results from preload compensation. Reviewing the videos and photos taken during the experiments reveals additional slipping effects of the blade within its clamping, causing sudden, minor decreases in the applied load.

In general, all blades withstood the expected maximum operational load at design point speed, given above in Equation (3). In all cases that a damage pattern became visible, causing the final, massive load decrease, it could be classified as delamination at the transition from blade to blade root at the trailing edge (see Figure 7).

Therefore, the safety factors S summarized in the first line of Table 5 are calculated from the maximum measured load, depending on the lowest- and highest-strength blade as well as averaged over all blades, and the estimated operational load at the transition between blade and root, determined above in Equation (3).

Noteworthy is the case of blade number 6, considered the most critical scenario due to its notable deviation from the other samples, achieving a maximum of $F_{max} = 3280$ N only. Nonetheless, it maintains a safety factor of 2.11, allowing it to withstand the force. If the rotational speed is increased to 120%, the increased load estimation of $F = 2239$ N

decreases this safety factor to only 1.47, allowing it to withstand the force, albeit with a marginal reserve. However, a safety factor of $S_{bending} > 14.9$ could be determined within the bending test, derived from the most conservative force calculation at the design point.

Table 5. Safety factors S and calculated averaged slopes $(\frac{ds}{dF\,dr})$ depending on the considered blades.

Parameter	Lowest Strength Blade	Average	Highest Strength Blade
S	2.11	3.24	4.56
$(\frac{ds}{dF\,dr})_l$ in $\frac{1}{N}$	$1.2 \cdot 10^{-5}$	$8.35 \cdot 10^{-6}$	$4.74 \cdot 10^{-6}$
$(\frac{ds}{dF\,dr})_u$ in $\frac{1}{N}$	$4.55 \cdot 10^{-6}$	$3.92 \cdot 10^{-6}$	$3.3 \cdot 10^{-6}$

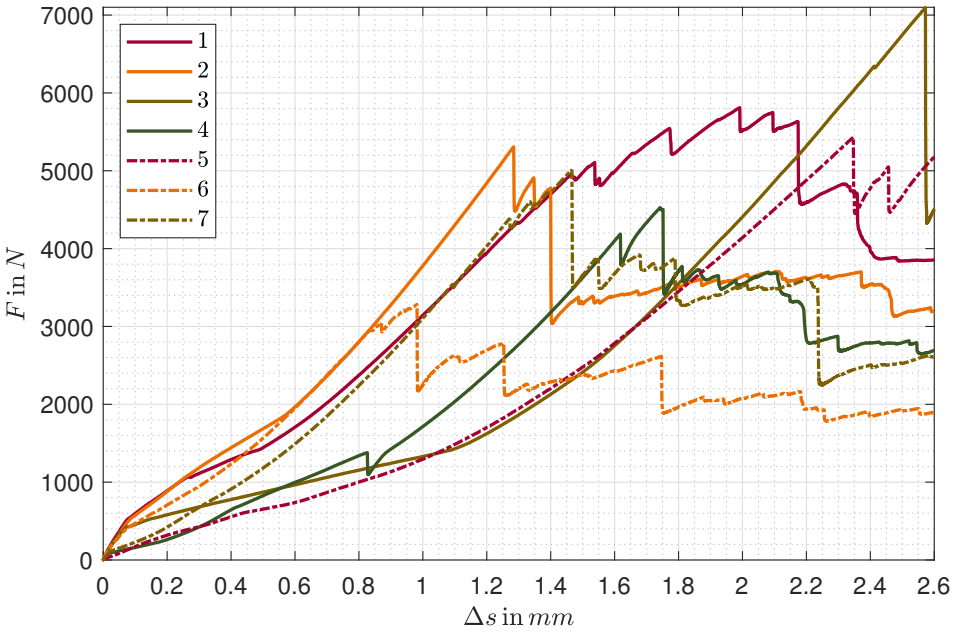

Figure 6. Elongation of the seven blades that received the same curing conditions depending on the applied load.

Figure 7. Typical damage pattern of delamination within the red circle at the blade's backside transition from the root into the actual blade.

Returning to the tensile testing, a specific *Young's modulus* cannot be calculated since the blade's cross-section varies across its radial extension, whereas the elongation Δs was measured over the entire blade only. However, averaged slopes $(\frac{ds}{dF\,dr})_i$ can be determined from the measured elongation and load as well as the radial extension of the blade $\Delta r = r_c - r_{hub}$, where r_c represents the radius of the outer clamping. These slopes are separated into two cases, as discussed above. On the one hand, the lower gradient $(\frac{ds}{dF\,dr})_l$ represents the initial, shallow slope measured during tensile tests. On the other hand, the upper,

steeper slope is described by $(\frac{ds}{dF\,dr})_u$, based on the assumption that the clamping effects do not occur during operation. Both cases are evaluated, summarized in the lower part of Table 5, and utilized to calculate the expected blade elongation Δs as follows:

$$\Delta s(\omega, r_j) = (\frac{ds}{dF\,dr})_i \cdot \int_{r_{hub}}^{r_j} F(\omega, r)\,dr \tag{4}$$

assuming that the considered $(\frac{ds}{dF\,dr})_i$ is the same for all radial positions and applying Equation (2) to calculate the individual elongations of each increment dr at radius r. The resulting tip clearances depending on the relative engine speed with regard to the design point speed are plotted in Figure 8, evaluated for an initial TC_0 of 1 mm under installation conditions. The error bars are formed by the results of the lowest- and highest-strength blades, respectively.

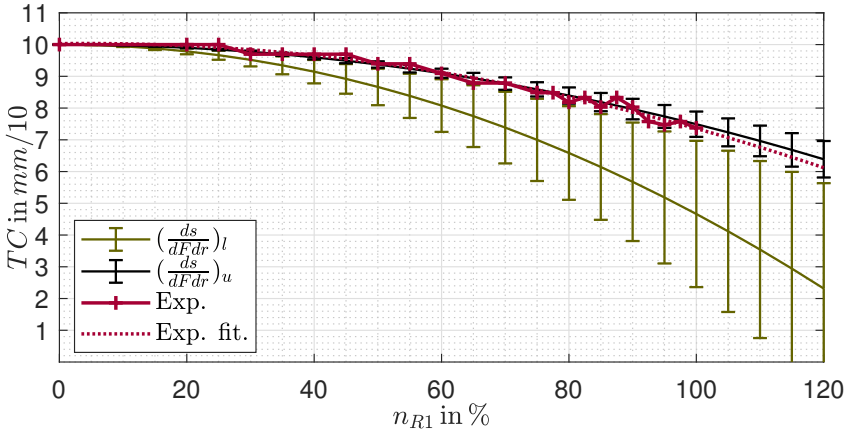

Figure 8. Experimentally measured tip clearance depending on the actual engine speed n, compared to the expected results from the tensile tests based on Table 5.

It can be inferred that at $n_{DP} = 100\%$, an elongation between 0.49 mm and 0.23 mm is present on average, considering the lower and upper slopes.

These results pave the way for engine testing in terms of a tip clearance measurement. The utilized high-speed camera, *FASTCAM Mini AX200*, was positioned in front of the engine. For these tests, the engine was not equipped with its standard inlet but with a similar one having a smaller axial length.

This enabled us to capture the tip clearance within the red square depending on the engine speed, as shown in the upper part of Figure 9. A frame rate of 120 kfps, a zoom lens, and an additional lighting source behind the engine facilitated analyzable shots. From the videos of the individual speeds, those photos were selected where the individual blades are at the same circumferential position to ensure comparability. The actual tip clearance was determined from the calibrated length between two reference positions at the casing and at the blade's tip, shown in the bottom part of Figure 9. Furthermore, the captured videos were evaluated for critical flutter effects, differing elongations of the individual blades, or misbalancing not detectable within the former static balancing. However, none of these phenomena occurred.

In order to definitely avoid contact with the casing, a conservative grinding of the blades' tips was conducted to achieve a tip clearance TC_0 under installation conditions of 1 mm. The actual measured tip clearance and a resulting exponential fitted curve are included in Figure 8 as solid and dotted red lines. On the one hand, there is a good agreement between the measured elongation and the calculated values based on the upper, larger gradient measured by the tensile tests, though the calculations seem to underestimate the actual elongation slightly. Three possible assumptions could be considered for this deviation. First, it appears reasonable that the density within the actual blade area is higher than that of the root due to the fleece used within it. Second, the blades are slightly thicker

than initially designed, as discussed previously. Both would result in higher centrifugal forces and therefore larger elongations when assuming that the deviating thickness results from additional resin, which only increases mass but does not bear significant loads. In addition, the calculated slopes are averaged over both the actual blade and the transition zone. Due to the strong curvature of the transition in comparison with the plane structure of the actual blade, it can be expected that their slopes vary widely. On the other hand, the resulting tip clearance at design point, approximately 0.74 mm, is larger than the initially specified value of 0.5 mm and further discussed below within the context of the CFD validation.

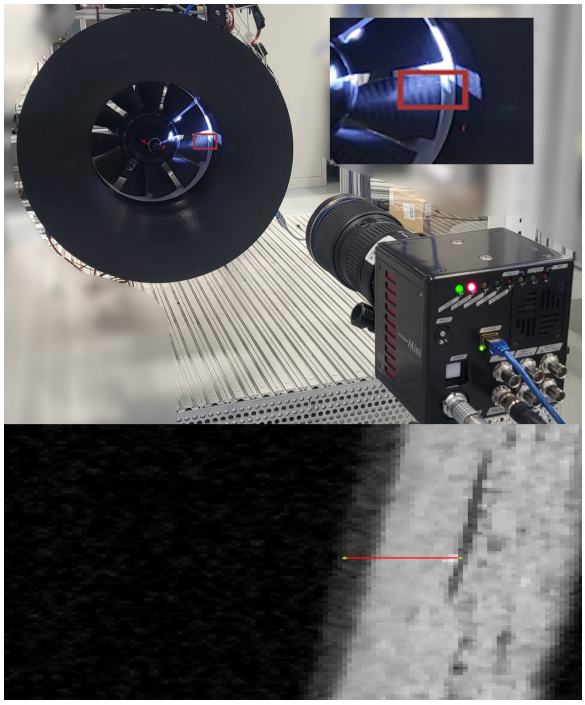

Figure 9. Tip clearance quantification by a high-speed camera.

Nevertheless, the test procedure seems to be a suitable indicator to predict the actual operational behavior. Even if the potential range of expected tip clearances appears to be large and requires careful commissioning tests of the engine, including a tip clearance measurement, the calculations could be used to determine more appropriate values for TC_0 than set here. To improve the calculation accuracy further, the elongations of the different zones should be measured individually due to their substantial difference in ply structure, for instance, by optical measurement systems. Furthermore, elongations of the inner disk were excluded and may account for deviations between the tensile test and experimental results, too. Addressing the second research question raised above, it can be summarized that the design, manufacturing, and commissioning of composite blades became feasible. Key factors are the direct integration of the manufacturing procedure into the design tool itself and the utilization of innovative approaches like the 3D-printed mouldings, reducing the manufacturing effort massively. Furthermore, the safety factors calculated above indicate a safe operation over a wide range of engine speeds and the test procedure could be verified. However, the higher total pressure ratio of the future contra-rotating propulsor requires larger engine speeds. To account for the subsequent higher loads, the blade design, especially the layer structure, should be optimized. To improve the design procedure, the test results could be utilized to set up a detailed FEM model that takes the individual ply orientation and anisotropic material characteristics of a composite structure into account. Furthermore, further comparisons of different blade curings or the selection of other materials of both resin and actual fabric seem to be beneficial. However, a composite rotor could be successfully manufactured, compared to the initial CAD rendering

in Figure 10. Within the following, it will now be examined whether this composite rotor compromises the design tool validation.

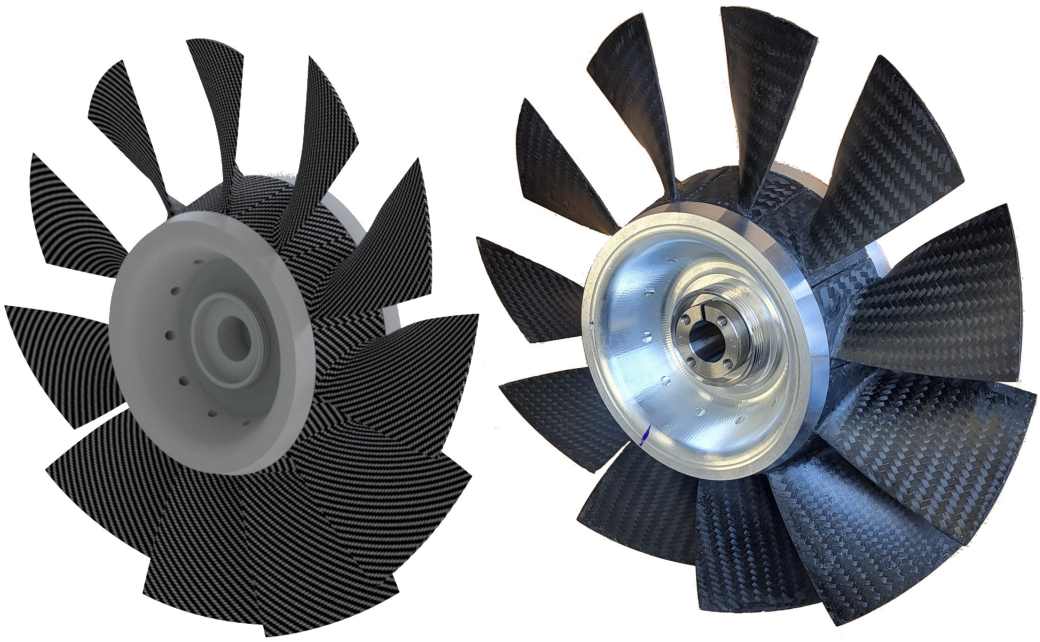

Figure 10. Comparison of the rotor design (CAD rendering, (**left**)) and the manufactured composite rotor (**right**) of the reference engine.

4. Experimental Setup of the Tool Validation

Apart from the rotor being the engine's main component, the nozzle and the test bed are discussed briefly in the following, as they are the key elements enabling the actual design tool validation. In addition to the actual design point calculation, considered by the tool as discussed at the beginning, the operating behavior at off-design points is of particular relevance. For axial compressors and fans, the operating point of highest efficiency is typically close to the surge limit. However, typically less efficient operating points are chosen that have a larger margin to this limit [37]. As the later contra-rotating engine aims to enlarge the operating range towards more efficient operating points through targeted adjustment of operating parameters, especially the speed ratio, it is essential that not only the design point but also the off-design points are accurately represented using the CFD utilized for the design tool. Consequently, this will be revisited in the following experimental tool validation, too. Therefore, several fully 3D-printed outer nozzles with different sizes were printed. By taking pictures with a high-speed camera both in and out of operation and superimposing them, it could be validated that the size of A_9 stayed consistent during operation and testing. Those differently sized nozzles were also taken over into the CFD to simulate the engine behavior under throttled and unthrottled conditions.

The test bed built at the institute serves for both static engine testing and experimental measurements in a wind tunnel, particularly in conjunction with the *particle image velocimetry (PIV)* system, which is, however, not utilized for the results shown here yet. Furthermore, the test bed is designed not only for the current single-engine reference propulsion system but is also preconfigured for a future, dual-engine contra-rotating configuration. Its data acquisition system, based on *National Instruments (NI)* software and hardware, includes various modules for data collection. This includes an ambient temperature measurement using *PT100* sensors, a six-component strain gauge for force and momentum measurement along the engine's axes, and a digital pressure sensing system with a focus on absolute and differential pressure measurements. Having a rated accuracy of 0.1% full scale, the strain gauge can measure up to 1000 N, and the engine and the gauge

are horizontally orientated before testing. All pressure sensors are rated with an accuracy of 0.25% of their full scale, having an effective resolution of 12 bits. Whereas the absolute pressure can be obtained by a 0-to-1.6 bar absolute sensor with a resulting maximum error of 400 Pa, the differential sensor can measure up to 100 mbar, resulting in a maximum deviation of 25 Pa with a resolution of 3 Pa. The offset of all pressure sensors is regularly taken and compensated. Additionally, the absolute mechanical engine speed n is captured using a laser-based light barrier system, consisting of a hole within the spinner cone and an edge counting within a digital input module. Data are read from the *NI DAQ* system by a connected measurement and control PC running *LabVIEW*-based data acquisition and control software. All parameters are collected with an adjustable frequency; for the following, 15 Hz was chosen, as steady-state operation should be measured only.

Due to the static operation outside the wind tunnel for the following tool validation, the obtained static inlet conditions of temperature and pressure equal their total values T_{t0} and p_{t0}, respectively. According to the Mach number similarity, they are used to calculate the corrected engine speed $n_{\text{cor.}}$, as follows [37]:

$$n_{\text{cor.}} = n \cdot \sqrt{\frac{T_{ref}}{T_t}} \tag{5}$$

These calculations are performed using a reference temperature $T_{ref} = 284.77$ K and pressure p_{ref} = 95,232 Pa derived from the *ISA standard atmosphere* [23] at an altitude of 520 m, which equals the institute's altitude. Since those reference conditions were already set within the design tool as inputs as well as in the following CFD as boundary conditions on inlet and outlet surfaces, the mechanical design speed of 14,487 rpm equals the corrected design speed, stored within the control software. To enable operation at higher temperatures, resulting in higher mechanical speeds, a slightly oversized water-cooled brushless motor was selected and installed. It is powered by a water-cooled *electronic speed controller (ESC)*, which is, in turn, supplied by a 63 VDC power source capable of providing up to 15.3 kW. To accommodate future operation with two electric motors having a combined power of up to 30.6 kW, a second identical power supply unit is already integrated into the test bed. The ESC generates the required sinusoidal signal by selectively applying voltage to the motor's three phases, with the duty cycle of this signal determining the time-averaged voltage. The actual motor speed then results in accordance with the motor-specific *kV* rating. However, the actual speed is governed by further factors, such as motor heating or the internal resistance of cables and the motor. The ESC is controlled via a *PWM* (*pulse width modulation*) signal from the *DAQ* (*data acquisition*) system, with the duty cycle regulated by the measurement and control system to maintain a constant corrected speed set by the user.

To protect the various sensor cables from the strong magnetic field of the motor supply, shielded cables are exclusively used. Mass flow rate is calculated from the differential pressure, measured between the engine's inlet and the ambient, and the cross-sections inlet and is corrected similar to the engine speed, as shown above [37]:

$$\dot{m}_{\text{cor.}} = \dot{m} \cdot \sqrt{\frac{T_t}{T_{ref}}} \cdot \frac{p_{ref}}{p_t} \tag{6}$$

Additionally, the total pressure difference to ambient can be measured within the engine using a radial traversing unit, enabling the calculation of area-averaged values. This unit is equipped with a calibrated, miniature five-hole probe from *Vectoflow*. This probe features five pressure ports in its head, allowing the determination of both total pressure and flow angles. Whereas the propulsor with the entire measurement equipment is shown on the left-hand side of Figure 11, the five-hole probe at a radial position of 50% is depicted on the right-hand side.

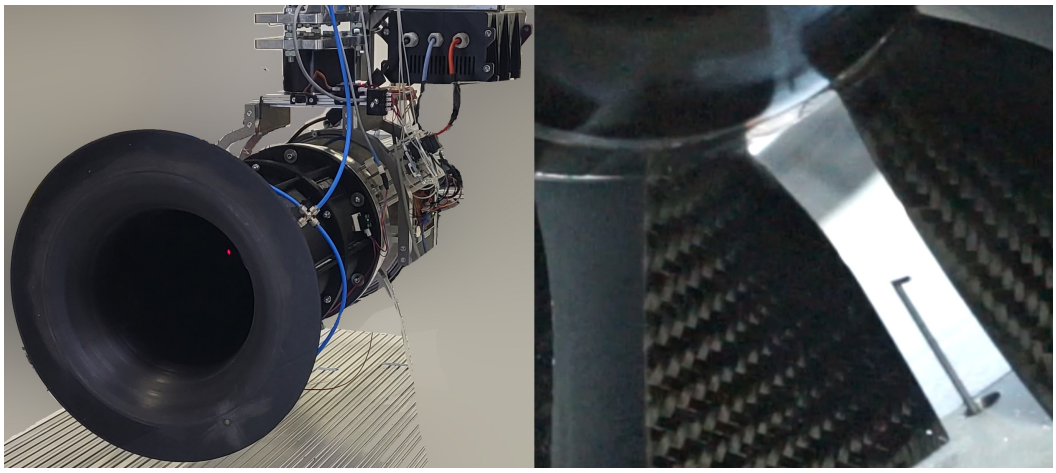

Figure 11. Propulsor within the static test bed, including the measurement equipment (**left**), and the utilized five-hole probe (**right**).

5. Results: Design Tool Validation

To validate the design tool, the engine's operation was investigated both in CFD and experiment not only at design point, corresponding to a nozzle cross-section of 100%, but also in throttled and unthrottled conditions by adjusting the nozzle's outlet area between 75% and 120%. Furthermore, four different corrected engine speeds of 40%, 60%, 80%, and 100% were evaluated, referring to the design point speed specification initially given in Table 1. Those operation points are summarized in Table 6.

Table 6. Overview of the operation points both simulated and experimentally measured, given in percent and referring to the design point nozzle opening and design point-corrected engine speed.

Parameter	Min. Value	Max. Value
Nozzle area in %	75	100
Corrected speed in %	40	100

In the experiment, the traversing unit was utilized at each operation point to determine the total pressure at 30 radial positions behind the rotor with a higher resolution close to hub and shroud, as shown in Figure 12, discussed in detail later. At each radial position, 50 samples were captured with 15 Hz, averaged and used to calculate an area-averaged total pressure increase and total pressure ratio of the position after the rotor against ambient, since the conditions in front of the rotor cannot be measured. To ensure comparability, the traversing's axial position aligns with the CFD's interface between the rotor and stator domains. Similarly, the CFD is also evaluated at 318 uniformly distributed radial positions, each averaged over the domain circumference, and the total pressure difference and ratio between this station at the rotor's outlet and the set pressure of the overall inlet were calculated.

To begin with the validation, the design point results are compared in Table 7, on one hand, based on the absolute values of total pressure increase $\Delta p_{t,\mathrm{R},0}$, and on the other hand, using relative errors e_r with regard to the experimental results.

In order to establish comparability here, too, the initially specified π_R is multiplied by the final iterative design process's value of π_{inlet} to receive the corresponding pressure increase, given in the first line of Table 7. Although the initial specification corresponds to a mass flow-averaged value due to the implemented calculation rules and, therefore, comparability is not necessarily guaranteed, it is in good agreement with the experimentally determined value, with a deviation of 0.1%.

Table 7. Comparison of total pressure ratio and total pressure increase, including the initial specification and the CFD and experimental results.

Case	$\Delta p_{t,\mathrm{R},0}$ in Pa	$e_{r,\Delta p_{t,R1,0}}$
Initial sp.	5938.9	0.1%
CFD Mesh 3, st.st.	5965.7	0.36%
CFD Mesh 2, st.st.	5868.8	1.27%
CFD Mesh 2. tr.	5893.8	0.85%
Exp.	5944.3	–

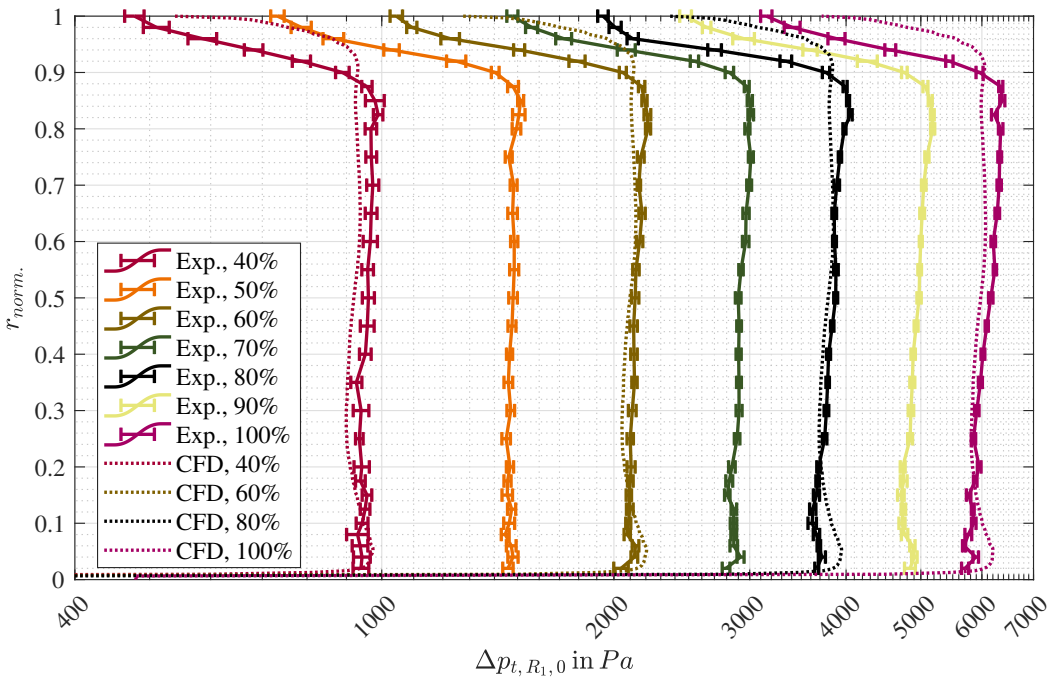

Figure 12. Total pressure increase from ambient to the measurement position depending on the normalized span. Nozzle opening equals design point cross-section. Comparison of CFD and experimental results at different corrected speeds, referring to design point speed, and including standard deviations.

The three different CFD results seem to be in contradiction to the abortion criterion of the iterative design process, requiring a deviation of less than 0.1% from the initial specification, as discussed above. However, during this process, a mesh slightly finer but geometrically similar to the third considered mesh was steady-state-simulated, with mass flow evaluated, averaging over the rotor only, undercutting the abortion criterion. The CFD results deviate from each other in accordance with the discussions above, but the deviations of all of these considered simulations from both the experiment and the initial specification are small.

This seems to confirm that the second mesh was a suitable selection for simulating the engine's performance map, plotted against the experimental results in Figure 13.

In general, the measured throttle curves of the RPS comply with the expected counterplay of mass flow and total pressure ratio. Especially the unthrottled performance at 110% and 120% nozzle opening is very well represented by the CFD, but also, the design operating line exhibits minor deviations only from the experimental results, even apart from the previously discussed design point.Like the relative deviation of the corrected mass flow, the deviation of the total pressure increase between CFD and experiment decreases from 2.03% at 40% corrected speed to 0.85% at 100% speed. Since the CFD simulations were carried out with the design point clearance of $\mathrm{TC}_{DP} = 0.5$ mm always, whereas the tip

clearance decreases in real operation from 1 mm at standstill to ≈0.74 mm at 100% speed, in accordance with the measurement carried out above, one could expect a decreasing deviation, as described. However, the chosen second mesh cannot confirm this tip clearance effect, as the simulated pressure ratio at design point operation is not larger, as expected from a smaller clearance. Returning to Table 7, the third mesh may be capable of mapping this effect, resulting in a larger total pressure increase, but such detailed investigations of flow phenomena are not required for the tool validation carried out here.

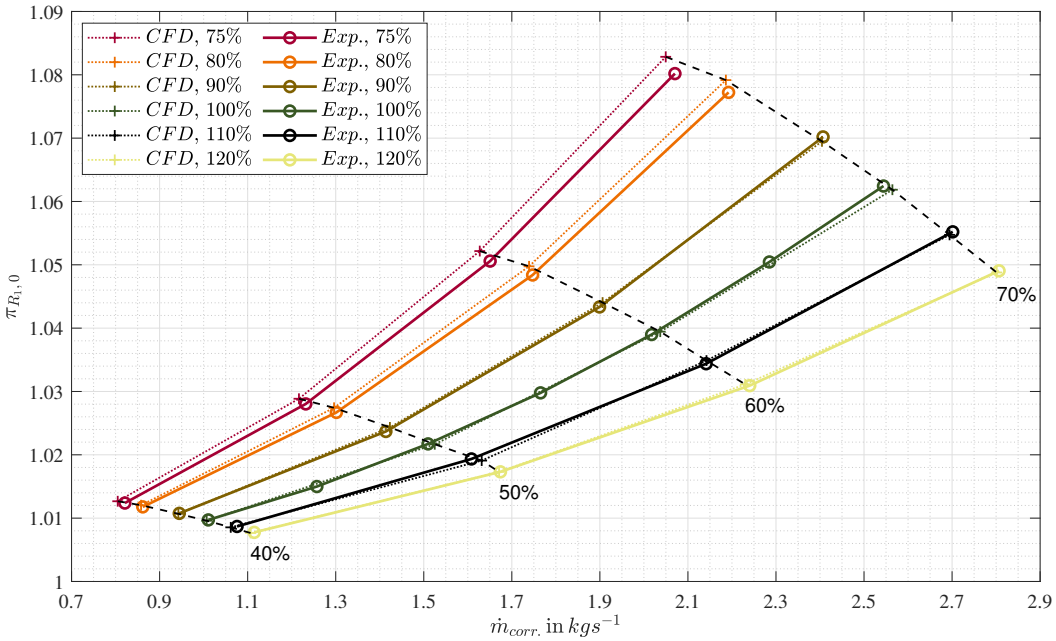

Figure 13. RPS performance map, including CFD and experimental results of total pressure ratio and corrected mass flow at different corrected engine speeds, given within the map, and six different nozzle openings from 75% to 120%, given within the legend.

The smaller the nozzle's cross-section, the higher the pressure build-up within the engine and the smaller the corrected mass flow $\dot{m}_{corr.}$. This directly influences the fluid's angle of incidence i against the blades. If this angle is too high or too low, a flow separation or even a stall on the fan blades can be the result. In the ideal case, without losses, the resulting throttle curves would be straight lines. However, apart from the losses caused by a deviating angle of incidence, the real throttle curves are influenced by friction and tip clearance or slipping effects [37], but the surge line was not yet reached by a nozzle opening of 75%. However, even the simulation of these throttled operation points seems to be feasible by the transient simulation approach, though the deviations increase towards more throttled operation points, reaching a maximum of 4.6% at 100% corrected speed and 75% remaining nozzle opening. Since the design tool is intended for future use in designing a fan with a higher pressure ratio, particularly concerning the throttled condition, it seems sensible to re-examine whether the increased computing effort of a finer mesh may be justified in order to potentially achieve higher accuracy.

Apart from the actual performance chart, a radial comparison of the total pressure increase is plotted in Figure 12. For all radial positions, there is a low standard deviation in a range of 23 to 30 Pa, which falls within the measurement deviation of the utilized digital differential pressure sensors. The original design based on the free vortex design principle is apparent in the CFD results through the nearly constant total pressure increase over a wide range of the normalized span, approximately from 5% to 90%. This is also evident in the experimental data up to a radial height of 85%. Both CFD and experimental data show a significant drop in total pressure increase in the span range close to the blade's tip, likely attributable to clearance losses and blade tip vortex effects. Given that the probe can

be precisely positioned by using a stepper motor for the drive, the simulation appears to underestimate the tip losses, as the drop in total pressure increase starts at a larger radial position. Similar results were already highlighted in the previous project, as described in [22]. Additionally, it was assumed that steady-state simulations might overestimate the influence of the tip vortex or that the measurement equipment was not able to capture it due to the transient nature of this phenomenon. In contrast, there is a measurable slight increase captured by the measurements of the RPS in total pressure in a radial range of 80% to 85%, just below the significant drop. The transient simulation results also show a similar, but minor and radial shifted increase. Though the drop close to the tip appears to be underestimated for the transient simulation applied here, too, the difference between simulation results and experimentally recorded data is much smaller than the observed differences compared to steady-state simulation results in [22].

Overall, the chosen simulation approach seems to be suitable to map the RPS performance characteristics accurately; the deviations between CFD and experimental data are within an acceptable range in order to consider the tool to be validated. In addition to the discrepancies in tip clearance already discussed, further geometric deviations may contribute to the discrepancies between CFD and experimental results. As mentioned earlier, the actual blade is thicker and has a shorter chord length compared to its CFD counterpart due to manufacturing tolerances. Nevertheless, the found composite manufacturing process does not seem to compromise the tool validation and experimental verification of the design approach, though it has to be further discussed in the context of future, aerodynamically higher-loaded blades. Other factors that could contribute might include rougher surfaces than assumed in the CFD, the application of *mixing plane* or *transient rotor–stator* approaches, or the modeling of only one and two blade passages, respectively.

6. Discussion and Conclusions

Returning to the initial research questions, a design and manufacturing process for carbon composite blades feasible for use within the university context and not compromising the tool validation was developed, enabling future transferable research. This was facilitated by the two key factors, utilization of $3D$-printed mouldings and ply creation directly integrated into the design tool. Further improvements regarding the geometric tolerances can be expected from the application of a newer, state-of-the-art resin. The tensile tests carried out were evaluated regarding the blade load assumptions, based on the tip clearance measured during operation. The data of these tensile tests should be used to validate a detailed FEM model. To utilize the composite blades for the future, contra-rotating propulsor and its mechanically higher blade loads, this model should be used to optimize the ply structure.

The tool's iterative character, including CFD simulations, as anticipated, improves the accuracy massively compared to an empirical formulation-based tool. The deviations between the initial specification and both the CFD and experimental data were reduced to a small percentage range, even though the manufactured composite blades deviate slightly from the initial design.

The application of transient CFD simulations improves the simulation accuracy for off-design operation points, especially in throttled operation. Since the computational effort is similar to the previously used steady-state simulations, this simulation type is utilized for prospective applications of the iterative design tool. However, the application of a finer mesh may be reasonable in spite of the higher computational effort. Particularly for the future contra-rotating engine, it seems sensible to set the iteratively found deviation angles at more than three radial positions. This will minimize the deviations between the specified and actual inflow into the second rotor over a wider range of the span. Further discussions of flow phenomena appears to be useful to improve simulation accuracy, for instance, by the utilization of the institute's particle image velocimetry system. Since the tip clearance seems to have a large impact on the engine's performance, it should be considered depending

on engine speed during simulation by incorporating the already mentioned detailed FEM analysis. Within the context of future research on this newly available propulsor, the differences between simulations and experimental results at operation points with a large tip clearance aim for an active tip clearance control which may improve the propulsor's performance. Both the design tool and the manufacturing process of composite blades will now be utilized to extend the operation range of electric aircraft engines by designing freely scalable contra-rotating, ducted engines.

Author Contributions: Conceptualization, S.H. and A.H.; methodology, S.H., A.H. and L.R.; software, S.H., L.R. and H.B.; validation, S.H.; formal analysis, S.H.; investigation, S.H. and A.H.; resources, S.H. and H.B.; data curation, S.H. and L.R.; writing—original draft preparation, S.H., L.R. and H.B.; writing—review and editing, S.H. and A.H.; visualization, S.H. and L.R.; supervision, A.H.; project administration, A.H. and S.H.; funding acquisition, A.H. All authors have read and agreed to the published version of the manuscript.

Funding: This publication is funded by the project *Electric Aircraft Propulsion—safe, efficient, digitally linked (ELAPSED)* within the cluster *dtec.bw—digitalization and technology research center* of the federal armed forces of Germany, which we gratefully acknowledge. The cluster dtec.bw is funded by the European Union—NextGenerationEU.

Finanziert von der Europäischen Union
NextGenerationEU

Data Availability Statement: The data presented in this study are available in the article.

Conflicts of Interest: The authors declare no conflicts of interest.

Abbreviations

The following abbreviations are used in this manuscript:

0	ambient conditions
1.1	inflow rotor
AS	axial spacing
F	force
FDM	fused deposition modeling
IPS	innovative propulsion system
K	construction angle
Ma	Mach number
ML	mean line
P	power
R	rotor
RPS	reference propulsion system
S	safety factor
SLA	stereolithography
TC	tip clearance
cor.	corrected
d	profile thickness
h	Altitude
i	number of blades
i	incidence angle
is	isentropic
m	mass
n	rot. speed
p	pressure

p	percentage deviation
r	radius
s	chord length
t	split
t	total
β	rel. flow angle
δ	deviation angle
η	efficiency
π	total pressure ratio

References

1. International Energy Agency. Global Energy Review 2020. 2020. Available online: https://www.iea.org/reports/global-energy-review-2020 (accessed on 20 September 2023).
2. Royal Netherlands Aerospace Centre (NLR) and SEO Amsterdam Economics. Destination 2050: A Route to Net Zero European Aviation. 2021. Available online: https://www.destination2050.eu/ (accessed on 18 September 2023).
3. Adu-Gyamfi, B.A.; Good, C. Electric aviation: A review of concepts and enabling technologies. *Transp. Eng.* **2022**, *9*, 100134. https://doi.org/10.1016/j.treng.2022.100134.
4. Gray, N.; McDonagh, S.; O'Shea, R.; Smyth, B.; Murphy, J.D. Decarbonising ships, planes and trucks: An analysis of suitable low-carbon fuels for the maritime, aviation and haulage sectors. *Adv. Appl. Energy* **2021**, *1*, 100008. https://doi.org/10.1016/j.adapen.2021.100008.
5. Klöwer, M.; Allen, M.; Lee, D.; Proud, S.; Gallagher, L.; Skowron, A. Quantifying aviation's contribution to global warming. *Environ. Res. Lett.* **2021**, *16*, 104027. https://doi.org/10.1088/1748-9326/ac286e.
6. Sacchi, R.; Becattini, V.; Gabrielli, P.; Cox, B.; Dirnaichner, A.; Bauer, C.; Mazzotti, M. How to make climate-neutral aviation fly. *Nat. Commun.* **2023**, *14*, 3989.https://doi.org/10.1038/s41467-023-39749-y.
7. Kharina, A.; Rutherford, D.; Zeinali, M. Cost Assessment of Near and Mid-Term Technologies to Improve New Aircraft Fuel Efficiency. 2016. Available online: https://api.semanticscholar.org/CorpusID:113796297 (accessed on 10 September 2023).
8. European Commission, Directorate-General for Mobility and Transport, Directorate-General for Research and Innovation. *Flightpath 2050: Europe's Vision for Aviation—Maintaining Global Leadership and Serving Society's Needs*; Publications Office: Luxembourg, 2011. https://doi.org/10.2777/50266 (accessed on 10 September 2023).
9. Publications Office of the European Union. Communication from the Commission to the European Parliament, the European Council, the Council, the European Economic and Social Committee and the Committee of the Regions. 2019. Available online: https://eur-lex.europa.eu/legal-content/EN/TXT/?qid=1576150542719&uri=COM%3A2019%3A640%3AFIN (accessed on 10 September 2023).
10. ZeroAvia Inc. Truly Clean Aviation. https://zeroavia.com/ (accessed on 10 September 2023).
11. H2FLY GmbH. H2Fly Breaking the Hydrogen Barrier. Available online: https://www.h2fly.de/ (accessed on 10 September 2023).
12. Universitaet der Bundeswehr Muenchen. Forschungsprojekt ELAPSED. Available online: https://www.unibw.de/elapsed (accessed on 10 September 2023).
13. Rossow, C.; Wolf, K.; Horst, P. *Handbuch der Luftfahrzeugtechnik*; Hanser Fachbuchverlag: München, Germany, 2014.
14. Hawner, S.; Hupfer, A. Entwicklung eines CFD-Auslegungstools fuer ein gegenlaeufiges, elektrisches Fantriebwerks und Anwendung fuer eine Parameterstudie im Designpunkt. *DLRK 2022* **2022**. https://doi.org/10.25967/570146.
15. Carter, A.; Hughes, H. *A Theoretical Investigation into the Effect of Profile Shape on the Performance of Airfoils in Cascada*; Aeronautical Research Council (ARC), Report No. 2384; Ministry of Supply, National Gas Turbine Establishment: Farnborough, UK, 1946.
16. Carter, A. *The Low Speed Performance of Related Aerofoils in Cascade*; Aeronautical Research Council (ARC), Ministry of Supply, National Gas Turbine Establishment: Farnborough, UK, 1950.
17. Qiu, X.; Japikse, D.; Zhao, J.; Anderson, M.R. Analysis and Validation of a Unified Slip Factor Model for Impellers at Design and Off-Design Conditions. *J. Turbomach.* **2011**, *133*, 041018. https://doi.org/10.1115/1.4003022.
18. Schnös, M. Eine Auslegungsmethodik für Mehrstufige Axialverdichter auf Basis Einer Profildatenbank. 2020. Available online: https://elib.dlr.de/140758/ (accessed on 10 September 2023).
19. Lieblein, S.. Incidence and deviation angle correlations for comressor cascades. *ASME J. Basic Eng.* **1960**, *82*, 575–587.
20. Ebus, T.; Dietz, M.; Hupfer, A. Expermimental and numerical studies on small contra-rotating electrical ducted fan engines. *CEAS Aeronaut. J.* **2021**, *12*, 559–571. https://doi.org/10.1007/s13272-021-00517-7.
21. Ebus, T.; Dietz, M. Small electrically powered contra-rotating turbo fan engines for high-speed aircraft application. In Proceedings of the AIAA Scitech 2020 Forum, Orlando, FL, USA, 6–10 January 2020. https://doi.org/10.2514/6.2020-1617.
22. Ebus, T.; Dietz, M.; Hupfer, A. Detailed Performance Studies on a Small Electric-Powered Contra-Rotating Ducted Fan Engine. *J. Propuls. Power* **2024**, *40*, 62–73. https://doi.org/10.2514/1.B39046.
23. International Civil Aviation Organization. *Manual of the ICAO Standard Atmosphere, Extended to 80 Kilometres (262 500 feet)*, 3rd ed.; ICAO: Montreal, Canada, 1993.
24. Scholz, N. *Aerodynamik der Schaufelgitter*, 1st ed.; Verlag G. Braun: Karlsruhe, Germany, 1965.

25. Mistry, C.; Pradeep, A.M. Effect of variation in axial spacing and rotor speed combinations on the performance of a high aspect ratio contra-rotating axial fan stage. *J. Power Energy* **2012**, *227*, 138–146.
26. Lei, Y.; Ji, Y.; Wang, C. Optimization of aerodynamic performance for co-axial rotors with different rotor spacings. *Int. J. Micro Air Veh.* **2018**, *10*, 362–369.
27. Nayak, N.; Mistry, C. Criteria for selection of solidity in design of contra rotating fan stage. In Proceedings of the NAPC 2017, Kanpur, India, 15–17 March 2017.
28. Verein Deutscher Ingenieure. *Durchflussmessung mit Drosselgeräten. Blenden und Düsen für besondere Anwendungen*; Beuth-Verlag GmbH: Berlin, Germany, 1991.
29. Heinrich, M.; Friebe, C.; Schwarze, R. Experimental and numerical investigation of a gearless one-motor contra-rotating fan. *Proc. Inst. Mech. Eng. Part A J. Power Energy* **2016**, *230*, 467–476. https://doi.org/10.1177/0957650916633014.
30. Bardina, J.; Huang, P.; Coakley, T. Turbulence Modeling Validation, Testing, and Development. *NASA Tech. Memo.* **1997**, *110446*, 10-2514.
31. Celik, I.; Ghia, U.; Roache, P.; Freitas, C.; Coleman, H.; Raad, P. Procedure for estimation and reporting of uncertainty due to discretization in CFD applications. *J. Fluids Eng.* **2008**, *130*, 078001. https://doi.org/10.1115/1.2960953.
32. Abumeri, G.; Kuguoglu, L.; Chamis, C. Composite Fan Blade Design for Advanced Engine Concepts. NASA Technical Reports. 2004. Available online: https://ntrs.nasa.gov/api/citations/20040040080/downloads/20040040080.pdf (accessed on 10 September 2023).
33. Coroneos, R.M.; Gorla, R.S.R. Structural analysis and optimization of a composite fan blade for future aircraft engine. *Int. J. Turbo Jet-Engines* **2012**, *29*, 131–164. https://doi.org/10.1515/tjj-2012-0024.
34. DLR Institut für Antriebstechnik. CRISP II: Counter Rotating Integrated Shrouded Propfan II. Available online: https://www.dlr.de/at/desktopdefault.aspx/tabid-7162/11868_read-27991/ (accessed on 10 September 2023).
35. Schmid, T.; Lengyel, T.; Schmidt, T.; Nicke, E. Optimization of a carbon-fiber composite blade of a counter-rotating fan for aircraft engines. In Proceedings of the 13th European Conference on Turbomachinery Fluid Dynamics & Thermodynamics, Lausanne, Switzerland, 8–12 April 2019. https://doi.org/10.29008/ETC2019-432.
36. DIN. *DIN EN ISO 527-5: 2022*. Kunststoffe—Bestimmung der Zugeigenschaften—Teil 5: Prüfbedingungen für Unidirektional Faserverstärkte Kunststoffverbundwerkstoffe; Beuth-Verlag: Berlin, Germany, 2022.
This BibTeX entry captures the essential details of the standard, including the title, author, publication date, and DOI link for reference.
37. Rick, H. *Gasturbinen und Flugantriebe: Grundlagen, Betriebsverhalten und Simulation*; VDI-Buch, Springer: Berlin/Heidelberg, Germany, 2013.